Aalborg Universitet

AALBORG UNIVERSITY
DENMARK

Controlling factor for fracture resistance and ionic conduction in glassy lithium borophosphate electrolytes

Du, Tao; Chen, Zhimin; Liu, Han; Zhang, Qi; Bauchy, Mathieu; Yue, Yuanzheng; Smedskjær, Morten Mattrup

Published in:
Materials Today Energy

DOI (link to publication from Publisher):
10.1016/j.mtener.2023.101390

Creative Commons License
CC BY 4.0

Publication date:
2023

Document Version
Publisher's PDF, also known as Version of record

Link to publication from Aalborg University

Citation for published version (APA):
Du, T., Chen, Z., Liu, H., Zhang, Q., Bauchy, M., Yue, Y., & Smedskjær, M. M. (2023). Controlling factor for fracture resistance and ionic conduction in glassy lithium borophosphate electrolytes. *Materials Today Energy*, *37*, Article 101390. https://doi.org/10.1016/j.mtener.2023.101390

General rights
Copyright and moral rights for the publications made accessible in the public portal are retained by the authors and/or other copyright owners and it is a condition of accessing publications that users recognise and abide by the legal requirements associated with these rights.

- Users may download and print one copy of any publication from the public portal for the purpose of private study or research.
- You may not further distribute the material or use it for any profit-making activity or commercial gain
- You may freely distribute the URL identifying the publication in the public portal -

Take down policy
If you believe that this document breaches copyright please contact us at vbn@aub.aau.dk providing details, and we will remove access to the work immediately and investigate your claim.

Materials Today Energy 37 (2023) 101390

Contents lists available at ScienceDirect

Materials Today Energy

journal homepage: www.journals.elsevier.com/materials-today-energy/

Controlling factor for fracture resistance and ionic conduction in glassy lithium borophosphate electrolytes

Tao Du [a, d], Zhimin Chen [a, d], Han Liu [b, c], Qi Zhang [a], Mathieu Bauchy [b], Yuanzheng Yue [a], Morten M. Smedskjaer [a, *]

[a] Department of Chemistry and Bioscience, Aalborg University, 9220 Aalborg East, Denmark
[b] Physics of AmoRphous and Inorganic Solids Laboratory (PARISlab), Department of Civil and Environmental Engineering, University of California, Los Angeles, CA 90095, USA
[c] SOlids inFormaTics AI-Laboratory (SOFT-AI-Lab), College of Polymer Science and Engineering, Sichuan University, Chengdu 610065, China

ARTICLE INFO

Article history:
Received 22 June 2023
Received in revised form
6 August 2023
Accepted 18 August 2023
Available online 22 August 2023

Keywords:
Glassy electrolyte
Molecular dynamics simulation
Machine learning
Fracture behavior
Ionic conductivity

ABSTRACT

Glasses are promising candidates as solid electrolytes for all-solid-state batteries due to their isotropic ionic conduction, formability, as well as high chemical, thermal and electrochemical stability. However, their mechanical properties and ionic conductivity need to be improved. Here, based on molecular dynamics simulations and classification-based machine learning, we reveal that both fracture behavior and ionic conduction in glassy lithium borophosphate electrolytes are encoded in their static structures. By systematically varying the Li and B content, we demonstrate that the machine learning-based structural descriptor termed "softness" can be used as an indicator for both fracture resistance and ionic conductivity. The "softness" metric is calculated from the static local atomic environment, but well captures the long-term dynamics of individual atoms. Notably, the propensities for B atoms to undergo bond-switching (correlated with fracture) and for Li ions to migrate (correlated with ionic conductivity) increase with an increase in atomic softness. Specifically, the out-of-equilibrium interaction of B and Li with oxygen neighbors enhances the propensity for B and Li to undergo bond-switching or rearrangement when experiencing stimuli. These results enable finding the optimum chemical compositions for glassy solid electrolytes with high mechanical stability and high ionic conductivity.
© 2023 The Author(s). Published by Elsevier Ltd. This is an open access article under the CC BY license (http://creativecommons.org/licenses/by/4.0/).

1. Introduction

The development of renewable energy sources calls for more efficient and safer batteries for electrification of transportation and energy storage systems [1,2]. Lithium-ion batteries have received significant attention not only as a power source for portable electronic devices but also for large-scale energy storage applications due to their relatively high energy density, reliability, low cost, and cyclability [3–5]. However, lithium-ion batteries often suffer from safety issues and inadequate chemical and thermal stabilities [6]. Owing to these issues, the high performance all-solid-state batteries need to be developed, in which liquid electrolytes should be replaced with superior solid electrolytes [7].

Among the various solid electrolyte materials, glassy electrolytes typically present several advantages such as isotropic ionic conduction, no grain-boundary resistance, compositional variability, and improved formability compared to crystalline counterparts [8]. Generally, lithium-ion conductive glasses can be classified according to their composition such as sulfide, halide, and oxide glassy electrolytes [9–11]. Although sulfide glasses exhibit higher ionic conductivity than oxide glasses, they are difficult to be handled due to their chemical instability in air, high production cost and proneness to react with lithium metal [8]. The halide-based electrolytes can feature higher electrochemical oxidation stability than sulfide electrolytes, but usually suffer from high production cost and poor reduction stability [11,12]. In contrast, oxide glasses feature good chemical stability, low production cost, high recyclability and formability and have been intensively studied as the solid electrolyte in thin-film batteries [13,14]. The mechanical properties and ionic conductivity of oxide glasses are the main properties that need to be improved for their applications as solid electrolytes [15]. Specifically, the resistance to crack formation and propagation is critical, since the electrolyte needs to accommodate deformation associated with the volume change of the electrodes during charging and discharging. Cracking in the solid

* Corresponding author.
E-mail address: mos@bio.aau.dk (M.M. Smedskjaer).
[d] These authors contributed equally.

https://doi.org/10.1016/j.mtener.2023.101390
2468-6069/© 2023 The Author(s). Published by Elsevier Ltd. This is an open access article under the CC BY license (http://creativecommons.org/licenses/by/4.0/).

electrolyte phase will lead to an increased interface resistance and decreased ionic conductivity in the battery, and eventually battery failure. While the mechanical properties of glassy oxide electrolytes have not been well studied, numerous efforts have focused on improving the ionic conduction of oxide glasses [16].

In order to design and fabricate oxide solid electrolytes with improved mechanical properties and ionic conduction, the structure-properties correlations need to be understood. However, the structure of glassy electrolytes is intrinsically disordered. As a prototype of glassy electrolytes, lithium borophosphate (LiBP) glasses are promising candidates for thin-film solid batteries owing to their thermal, chemical and electrochemical stability [13,17,18]. Previous research suggests that the mixed network former effect by having both B and P units in LiBP glasses leads to improved thermal durability and ionic conduction [19,20]. The lithium ion conduction in LiBP glasses can be enhanced as the content of Li ions and thus non-bridging oxygens increases [17]. As another issue of oxide glasses, the crack behavior of glassy electrolytes has been rarely characterized and remains poorly understood [21]. As found in our recent study [22], the fracture behavior and Li transportation in LiBP glasses are governed by the bond-switching propensity of B atoms and medium range structure features, respectively. To enable the prediction of such properties, further work is needed to pinpoint the atomic-scale structural features governing ionic conduction and crack behavior.

Machine learning offers a promising opportunity to discover the hidden pattern in multidimensional data, which has made it possible to predict the dynamics of disordered materials (including cracking and diffusion behaviors) from their non-intuitive structural features [23–25]. To this end, a variety of machine learning algorithms have been applied, including support vector machine [24], logistic regression [26], graph neural network [27], convolutional neural network [28], etc. Among these, the non-intuitive structural fingerprint termed as “softness” proposed by Cubuk et al. has been found to be strongly correlated with the propensity of individual atoms to rearrange based on their local environment [24,29]. For example, in our previous work on disordered Al_2O_3, we found that the long-term dynamics of the atoms upon fracture is hidden in their initial static structure [25]. In addition to the fracture behavior, the ionic conduction is also strongly correlated with the atomic rearrangement. Indeed, the most commonly used mean squared displacement (MSD) metric to characterize ionic conductivity in atomistic simulations has been calculated based on atomic movement [30]. Therefore, an improved understanding of the structural features determining atomic rearrangement is essential for predicting both the mechanical properties and ionic conduction of glassy electrolytes.

In this work, we explore the structure-property correlation of glassy LiBP electrolytes using the machine-learning based “softness” concept. We use molecular dynamics (MD) simulations, validated by experiments, to obtain atomic scale information about the fracture and conductivity mechanism. Specifically, we focus on two series of glassy LiBP electrolytes, namely glasses with fixed B_2O_3 content ($(Li_2O)_{40+x}(B_2O_3)_{30}(P_2O_5)_{30-x}$) and glasses with fixed Li_2O content ($(Li_2O)_{40}(B_2O_3)_{30+x}(P_2O_5)_{30-x}$) where $x = -10, -5, 0, 5$, and 10. Each glass sample was named according to its composition, e.g., Li40B30P30 represents the glass composition $(Li_2O)_{40}(B_2O_3)_{30}(P_2O_5)_{30}$ (see Supporting Table S1). By isolating the relative effects of Li and B contents on the electrolyte performance, we correlate the fracture behavior and ionic conduction with the bond-switching activities of B and mobility of Li atoms, respectively. Given the simplicity and accuracy of the classification model, we have used a logistic regression classifier for the “softness” calculation as it makes the model interpretable to the input structural features. Based on this logistic regression classification model, we show that the propensity to bond switch or atomic rearrangement is encoded in the static structure of the electrolytes before any external stress or thermal excitation is applied. Based on the interpretable features of the applied logistic regression algorithm, we identify the most influential structural parameter of the radial order function controlling the atomic dynamic behaviors.

2. Results and discussion

2.1. Structural analysis of simulated glasses

We first characterize the atomic structures of glassy LiBP electrolytes. As a representative composition in both series of glasses, the atomic snapshot of a Li40B30P30 glassy electrolyte is shown in Fig. 1a including its structural units: Li ions, $^{[3]}$B triangles, and $^{[4]}$B and $^{[4]}$P tetrahedra, where $^{[n]}$X denotes the coordination state of the element X. The short-range order (SRO) and medium-range order (MRO) structures of the glassy electrolytes are characterized by calculating $D(r)$ and $S(q)$, respectively, from the MD simulations (see Methods section). We show the spectra for Li40B30P30 in Fig. 1b, for which the experimental data are also available in literature for this composition. The simulated $D(r)$ exhibits good agreement with the experimental result in terms of the position and relative intensity of the peaks based on our previous work [22]. Although there are some discrepancies regarding the second intense peak of $S(q)$ (the so-called principle peak), the main feature of the MRO structure, i.e., the first sharp diffraction peak (FSDP) of $S(q)$ is well reproduced. These results highlight that the MD simulations can reproduce the structural SRO and MRO features. The density evolution of the simulated glasses also agree well with the experiment values (see Supporting Fig. S1).

Fig. 1c shows the pair distribution function (PDF) $g(r)$ of the LiBP glasses for the different chemical compositions. All the LiBP glasses exhibit three main peaks, corresponding to the B–O/P–O, Li–O, and O–O bonds. For the glasses with fixed B_2O_3 content, the change in Li_2O content systematically alters the intensities of these peaks. In contrast, the first binary peak is mainly influenced by the compositional change in the glasses with fixed Li_2O content. From the partial PDF shown in Supporting Fig. S2, both systems exhibit a $^{[4]}$B-to-$^{[3]}$B conversion with an increased x value in $(Li_2O)_{40+x}(B_2O_3)_{30}(P_2O_5)_{30-x}$ and $(Li_2O)_{40}(B_2O_3)_{30+x}(P_2O_5)_{30-x}$. This is evidenced by the leftward shift of the first peak in $g_{B\text{-}O}(r)$, i.e., the decreased B–O distance. This finding agrees with the experimental results from Ref. [31] In contrast, the P–O distance does not exhibit significant changes with composition. The $^{[4]}$B-to-$^{[3]}$B conversion can also be observed from the increased coordination number (CN) of B and the increase in the O–B–O bond angle, as shown in Supporting Figs. S3 and S4, respectively. Fig. 1d shows the composition dependence of the MRO structure. The simulated structures of the LiBP electrolytes exhibit a lack of long-range order as observed from the diffusive scattering of the $S(q)$. The FSDP in $S(q)$ corresponds to the representative medium-range length scale. As the FSDP shifts to the higher q position with an increase in x, the structure is gradually densified, which echoes the molar volume changes shown in Supporting Fig. S5. That is, we observe that both the values and the composition dependency of density are well reproduced by the MD simulations. The increase of x leads to a more ordered phosphate tetrahedra structure as the O–P–O bond angle distribution becomes narrower while it maintains to be centered at 109° (Supporting Fig. S6). The fractions of different Q^n species of phosphate units (see Supporting Fig. S7) also exhibit the same dependence on composition as the previous experimental results for similar compositions [31]. Here, Q^n denotes a four-fold coordinated phosphorous unit connected by n bridging oxygens.

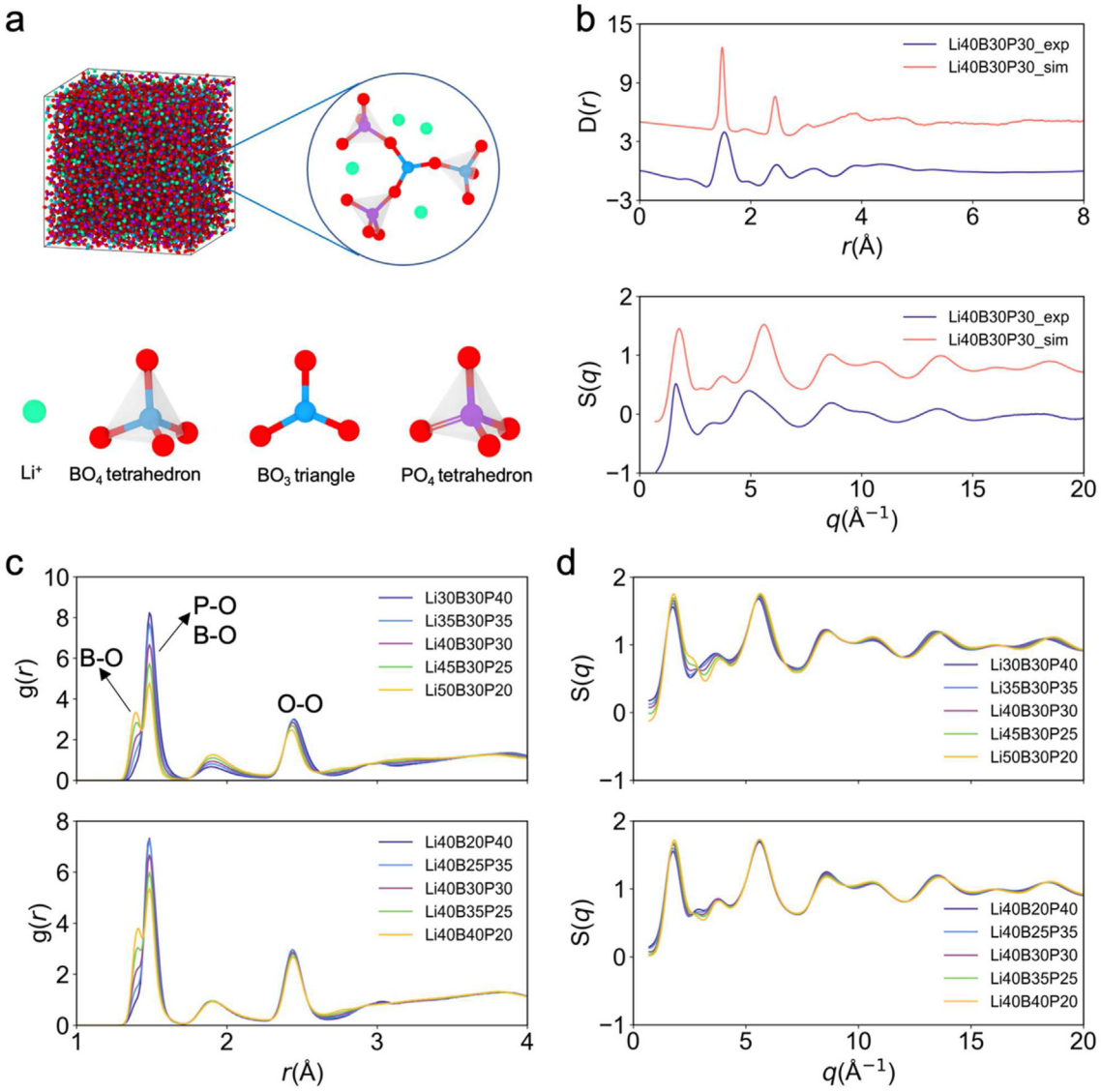

Fig. 1. (a) Atomic structure and photograph of Li40B30P30 glassy electrolyte. (b) Comparison of experimental (red) and simulated (blue) D(r) and $S(Q)$ of Li40B30P30 glassy electrolyte. The experimental data are taken from Ref. [22]. (c,d) Simulated (c) g(r) and (d) $S(Q)$ of LiBP glassy electrolytes with varying compositions. The detailed composition for each sample can be found in Supporting Table S1.

2.2. Mechanical properties

We analyze the mechanical response of the LiBP electrolytes during a simulated uniaxial tensile process. The stress-strain (σ-ε) curves of the compositions with fixed B_2O_3 content are shown in Fig. 2a. As expected, the increase in Li_2O content depolymerizes the network structure of the glass, thereby decreasing both strength and ductility. In contrast, the mechanical response of the glasses with fixed Li_2O content does not show any obvious composition dependence (Supporting Fig. S8). Since fracture processes are typically accompanied by changes in chemical bonds, the concept of bond-switching can be used to analyze fracture behavior [32]. As shown in Fig. 2b, the fracture of the LiBP glasses is accompanied by crack initiation and propagation. At a strain of 0.4, the sample is almost fractured with few B—O and P—O bonds bridging the crack.

The three types of bond-switching activities of B as a function of applied strain are shown in Figs. 2c—e. Compared to the non-strained structure, the B atoms can be subjected to bond-switching activities such as decreased CN, increased CN and swapped CN. Note that we do not show the bond-switching activities of P atoms here since they are negligible (Supporting Fig. S9). Among the three kinds of bond switching activities, the increased coordination number of B atoms shown in Fig. 2d is mainly attributed to the out-of-equilibrium state of $^{[3]}$B. These units tend to convert to $^{[4]}$B under deformation, and therefore contributes to the smallest extent to the total bond switching activities. The other two bond switching activities, i.e., decreased or swapped CN of B are closely correlated with the deformation process since they have the same dependence on the composition as the stress-strain responses, and they are the main reservoirs to dissipate the strain energy. Fig. 2c shows that the events of decreased CN increase initially with an increase of applied strain, but after reaching the maximum value, the number of events decreases and levels off upon the onset of fracture. In contrast, the increased and swapped CN activities increase monotonically with an increase in strain, which is attributed to glass relaxation, i.e., more increased and swapped CN events occur due to the partial re-densification of the glass induced by the stress release upon brittle fracture. Overall, the

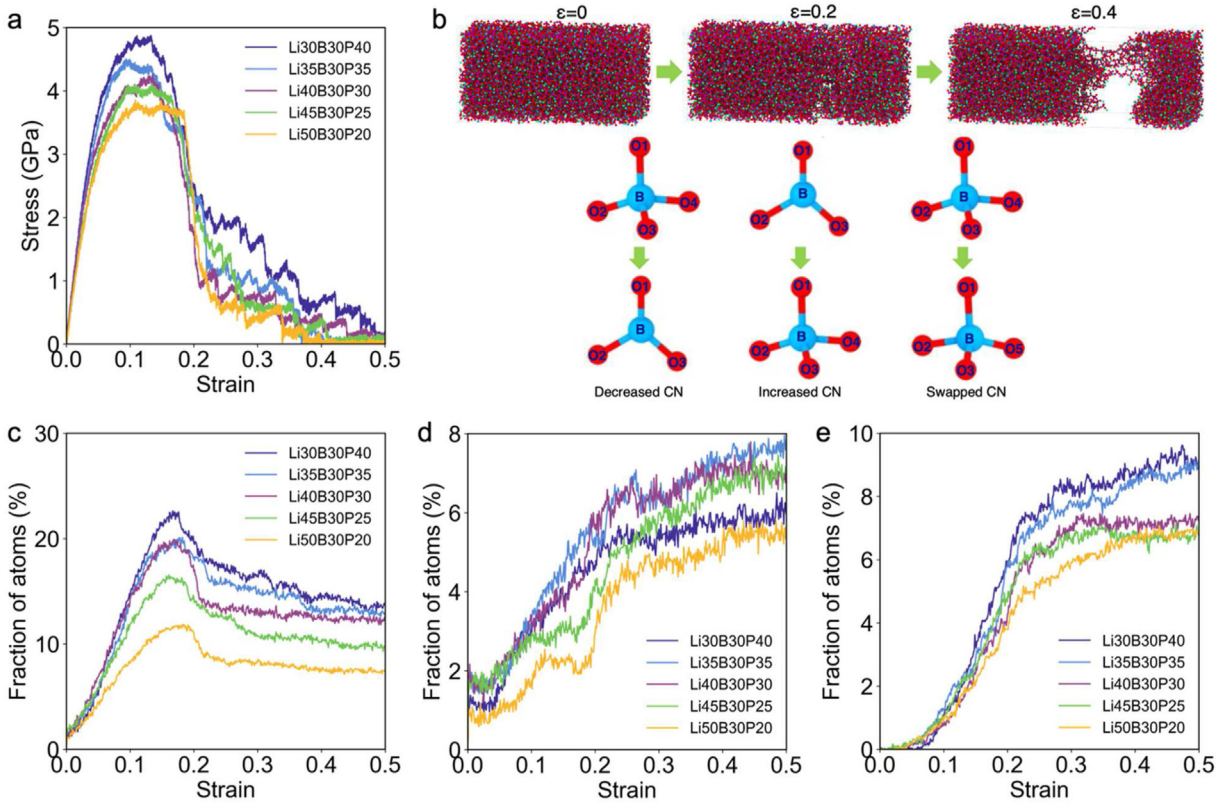

Fig. 2. (a) Stress-strain curves of glassy LiBP electrolytes with fixed B_2O_3 content. (b) Atomic snapshots of the fracture process and the three types of bond-switching activities for the Li40B30P30 composition at different strain values. (c–e) Fraction of B atoms subjected to (c) decreased CN, (d) increased CN, and (e) swapped CN as a function of applied strain for glasses with fixed B_2O_3 content.

bond-switching probability decrease with an increase of Li_2O content in the glassy LiBP electrolytes (Supporting Fig. S10). This tendency agrees well with the dependence of the mechanical response on composition. Next, we seek to predict the propensity of boron atoms to bond switch based on the non-strained glass structure, and thereby to predict the fracture behavior of LiBP glassy electrolytes.

2.3. Ionic conductivity

Since ionic conduction is another key performance for solid-state electrolytes, we analyze the dynamic and kinetic properties of the Li ions based on the MD simulations. Fig. 3a illustrates the trajectory of Li ions in the glassy Li40B30P30 electrolyte during the 300 K equilibration process. The white to green gradient lines highlight the positions of selected Li ions as a function of time. We observe that the dynamics of Li ions exhibits distinct behaviors, i.e., some Li ions are trapped in cages (immobile Li), while some can jump out of their local confinements (mobile Li). The latter Li ions promote the ionic conduction, and therefore, it is essential to understand the intrinsic mechanism governing Li^+ rearrangement. The MSDs of Li ions in glasses with fixed Li_2O content at 300 K and 800 K are presented in Figs. 3b and c, respectively. The MSD at 300 K does not exhibit obvious dependence on composition, since it does not reach the diffusive regime. When the samples are simulated at 800 K, the MSD values increase significantly with time. Meanwhile, both the MSD values at 300 and 800 K increase with an increase in the Li_2O content (Supporting Fig. S11), agreeing with measured ionic conductivities of Li_2O-rich glasses [17]. Additionally, the final MSD values exhibit a positive correlation with the B_2O_3 content, indicating a higher ionic conduction in the B_2O_3-rich electrolytes. Compared to the previous findings [13,22], our results show that the ionic conductivity will not only increase with an increasing Li content, but also increase with an increasing B content in the LiBP glasses.

Although the MSD results can be correlated with experimental observations, the MSD at 300 K cannot reach the diffusive regime [33] (i.e., with a slope of one in the log-log plot of MSD vs. time) within the simulation time accessible. To correlate the atomic rearrangement of Li at 300 K with the transport properties, we have calculated the cumulative nonaffine displacement (D_{cum}) of each Li ion during the 100 ps relaxation at 300 K (see Methods section). As shown in Fig. 3d, the D_{cum} values monotonically increase as a function of time, but the mobile Li ions systematically exhibit a higher D_{cum} value compared to the immobile Li ions over time. As such, the D_{cum} metric is a more robust indicator for rearrangement than the conventionally used MSD metric. A comparison of MSD and D_{cum} curves of individual Li ions during the 800 K equilibration also confirms the robustness of the D_{cum} metric (see Supporting Fig. S12). This is likely because, unlike the cumulative nonaffine displacement, MSD is affected by the reversibility (e.g., atom jumps to another pocket followed by another jump back to the original pocket) and directionality (angle between one jump and the following one) of the atomic jumps. The distributions of final D_{cum} values are shown in Fig. 3e and imply that glassy LiBP electrolytes with a high ion conductivity generally exhibit larger D_{cum} values. Interestingly, when comparing the MSD results at 800 K (Fig. 3c) with the D_{cum} distribution at 300 K (Fig. 3e), the spontaneous dynamics in the ambient environment are highly correlated with the diffusion behaviors at elevated temperature. That is, Li ions that

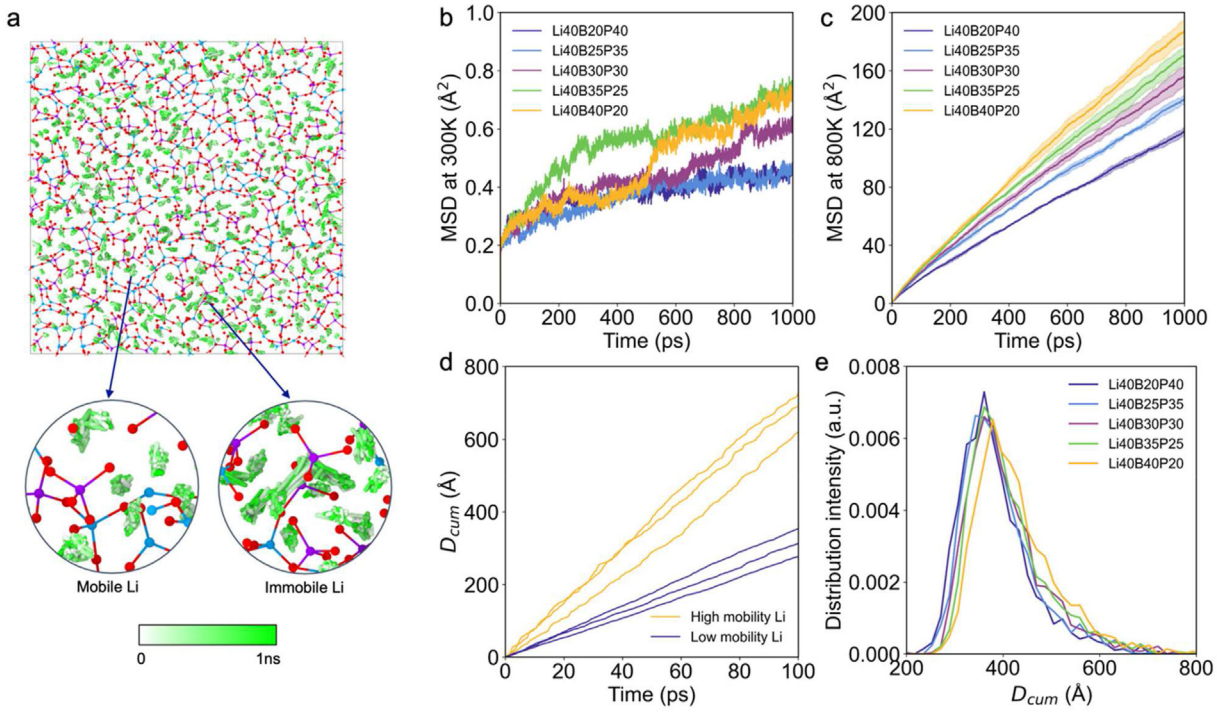

Fig. 3. (a) Atomic trajectories of Li ions in the Li40B30P30 glassy electrolyte during the 300 K equilibration process, which highlights the distinct propensities of Li to rearrange. The color coding of Li trajectories refers to the simulation time. (b,c) MSD of Li in LiBP glassy electrolytes with fixed Li_2O content at (b) 300 K and (c) 800 K. (d) Cumulative nonaffine displacement of selected Li atoms during the 300 K relaxation process. (e) Distribution intensity of cumulative nonaffine displacement of Li atoms after 100 ps relaxation at 300 K for the LiBP glassy electrolytes with fixed Li_2O content.

exhibit higher D_{cum} values yield a high ionic conductivity. Therefore, the final D_{cum} value of each Li reflects the atomic rearrangement and can be used as an indicator for ion conductivity.

2.4. Classification-based machine learning

Based on the above results, the fracture behavior and ion conduction are found to be correlated with P_{BS} (the probability to bond switch) of B atoms and D_{cum} (cumulative nonaffine displacement) of Li atoms, respectively. In the following, we investigate whether the propensity of B or Li atom to be mobile or immobile (i.e., the propensity to bond switch or rearrange) can be predicted based on the static glass structure. To this end, following the softness approach proposed by Cubuk et al. [29], we constructed a hyperplane using logistic regression to distinguish the rearrangement of atoms based on their structural features (Fig. 4a). The softness S is computed as the distance from the hyperplane to the position in the feature space. Herein, a positive value is associated with a mobile atom, while the absolute value indicates the probability of rearrangement. The detailed process and results of calculating softness can be found in the Methods section.

We first investigate the correlation between softness and atomic behaviors, i.e., bond-switching propensity and diffusion behavior. Interestingly, although the softness S is calculated based on the static structure, both the load- and time-induced dynamics of atoms are highly correlated with the softness values, yielding a predicting accuracy of around 0.77. Another interesting finding is that although this analysis relies on a classification model (wherein an atom can only be mobile or immobile), it eventually yields a quantity (structural descriptor) that is correlated to the rearrangement. Namely, previous investigations of alkali borophosphate glasses indicate the physical properties (e.g., the glass transition temperature, Vickers hardness, and liquid fragility) exhibit a highly non-linear correlation with composition [34]. Here, based on a classification model, we demonstrate that the long-term behaviors, i.e., bond-switching and diffusion properties exhibit an exponential dependence on S which also suggests that the quantity of S captures the activation energy of the process [26] since the softness concept is strongly correlated with the energy landscape associated with atomic dynamics [35]. Specifically, Li atoms with a large S are more likely to diffuse in the glass, while B atoms with a large S tend to experience bond-switching when the glass is subjected to deformation. We note that S is calculated based on the initial structure, whereas the D_{cum} values and bond-switching rate are computed at the end of the simulation (i.e., the glass is dynamically relaxed for 100 ps or the glass is stretched up to $\varepsilon = 1.0$). That is, the strong correlation between initial softness and atomic behavior clearly illustrates that the long-term behaviors of LiBP glasses are quantitatively encoded in their initial static structure.

The distributions of S of the Li atoms in the glasses with fixed Li_2O content are shown in Fig. 4c. We observe that the $\langle S \rangle$ of Li atoms systematically increases with an increase in the B_2O_3 content (inset of Fig. 4c), in agreement with the higher ionic conductivity observed in B_2O_3-rich LiBP glasses. Fig. 4d illustrates the distributions of S of B atoms in the glasses with fixed B_2O_3 content, where all the S distributions exhibit bimodal features. The two peaks are located at softness values of −0.4 and 0.6, respectively, indicating the distinct behaviors of immobile and mobile B atoms. As shown in the inset of Fig. 4d, the bimodal distribution originates from the different coordination states of B atoms, i.e., the $^{[4]}$B atoms are more prone to bond switch than the $^{[3]}$B atoms. With a decrease in the P_2O_5 content, the relative fraction of immobile B atoms increases at the expense of mobile B atoms, leading to the overall decrease of $\langle S \rangle$ of B atoms. This explains why LiBP glasses with a higher P_2O_5 content feature more pronounced bond-switching propensity, thus

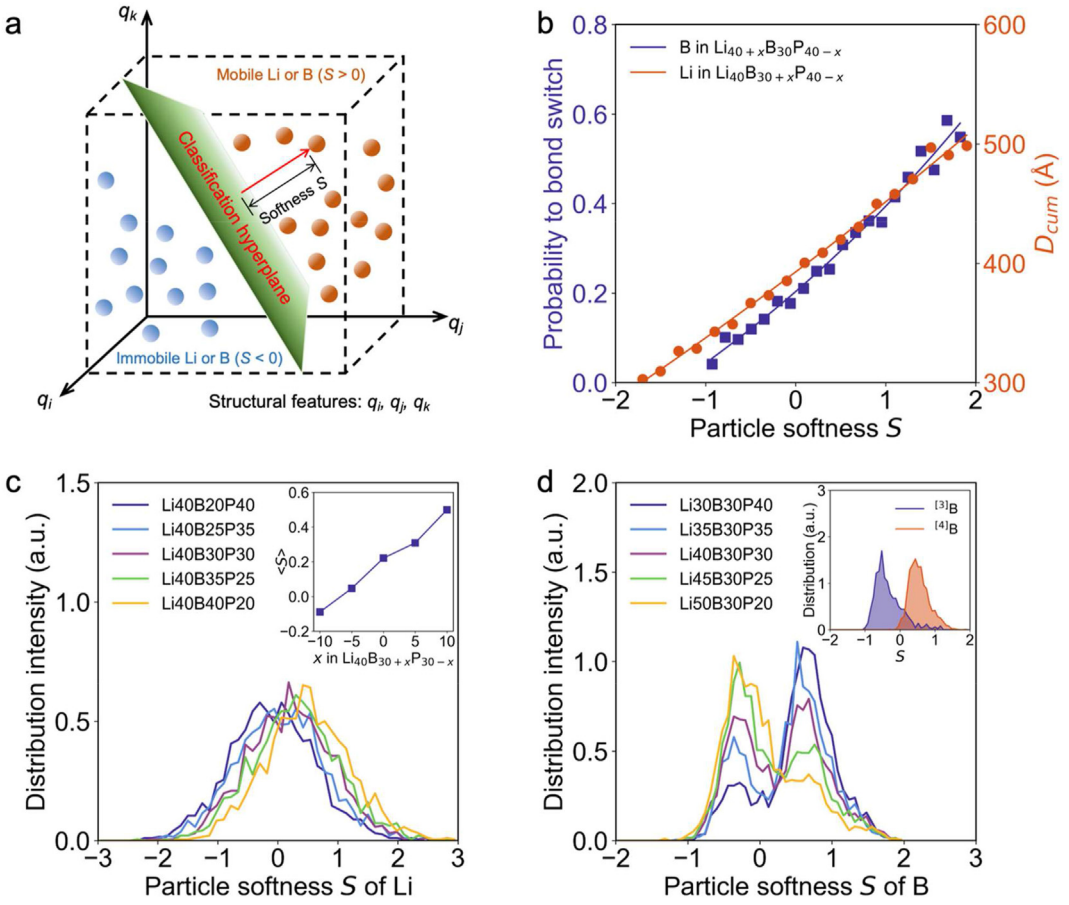

Fig. 4. (a) Schematic of the classifier hyperplane to determine the rearrangement tendency of atoms, i.e., B atoms with high rearrangement tend to experience bond-switching after deformation, while Li atoms with high rearrangement tend to diffuse spontaneously. (b) Probability of B atoms to undergo bond-switching and cumulative nonaffine displacement of Li atoms as a function of their softness. The lines are guides to the eyes. (c,d) Distribution intensity of the atomic softness of (c) Li in the electrolytes with fixed Li_2O content and (d) B in the electrolytes with fixed B_2O_3 content. The inset figure of Fig. 3c illustrates the <*S*> of Li in the electrolytes with fixed Li_2O content as a function of the glass composition. The inset figure of Fig. 3d shows the distribution of *S* of $^{[3]}$B and $^{[4]}$B in the Li40B30P30 glassy electrolyte.

exhibiting improved nanoscale ductility. Interestingly, although the coordination information is not directly provided in the input structural features to the machine learning model, the computed softness is able to capture the distinct dynamical behaviors induced by these coordination states.

2.5. Structural origin of softness

We then correlate the softness metric with other structural features such as coordination number and atomic volume to understand the real-space structural origin of softness. Fig. 5a shows the correlation between the atomic volume and softness for $^{[3]}$B and $^{[4]}$B atoms. Consistent with the softness distribution in Fig. 4d, $^{[4]}$B atoms tend to exhibit a higher softness than $^{[3]}$B atom, which highlights the importance of the first coordination shell of B atoms in governing their dynamical behaviors. Namely, $^{[4]}$B atoms with a lower atomic volume are subjected to a higher stress state, which can be released through the change of its CN under an external stimulus (Supporting Fig. S13). Based on the results in Fig. 5a, we find that the B atoms tend to decrease their coordination number with an increase in the atomic volume, while the B atoms with the highest softness are located in the transition state between $^{[3]}$B and $^{[4]}$B, namely, $^{[4]}$B with a high atomic volume or $^{[3]}$B with a low atomic volume. Since the atomic volume is governed by the bond length and CN, the B—O bond length may play an important role in governing the softness of B atoms. Furthermore, Li atoms with higher softness (i.e., higher rearrangement tendency) are typically associated with the Li atoms with larger atomic volumes, thus lower CNs. This correlation is consistent with the result in Ref. [26], which shows that particles with larger atomic volumes and lower CNs tend to exhibit higher rearrangement, thus highlighting the different origins of structural features in governing the fracture and diffusion behaviors.

To better illustrate the effects of atomic environment on the softness metric, we correlate the parameters of the logistic regression model with the atomic structure. Specifically, the logistic regression model trained only on the radial function enables the computed softness to be highly interpretable with the pairwise atomic correlations. According to Eq. (4) in the Methods section, the weight function $w(r)$ corresponds to the contributions of each feature of $G(i;r)$ to the classification. Therefore, the absolute value of $w(r)$ denotes the importance of $G(i;r)$ in the classification, while a positive or negative value of $w(r)$ represents that an increasing value of $G(i;r)$ tends to result in an increased or decreased softness value, respectively. As described in detail in the Methods section, $G(i;r)$ consists of the radial functions of four pairwise correlations (e.g., B—Li, B—B, B—O, and B—P when B is the focused element). For the softness calculation of B, the weight parameter $w(r)$ and partial pair distribution function of the four atom pairs are shown in Fig. 5c and Supporting Fig. S14. Among these pairs, the $w(r)$ of B—O pair exhibits the largest absolute value, i.e., the B—O interactions are the most influential features. As shown in the lower panel of Fig. 5c, the

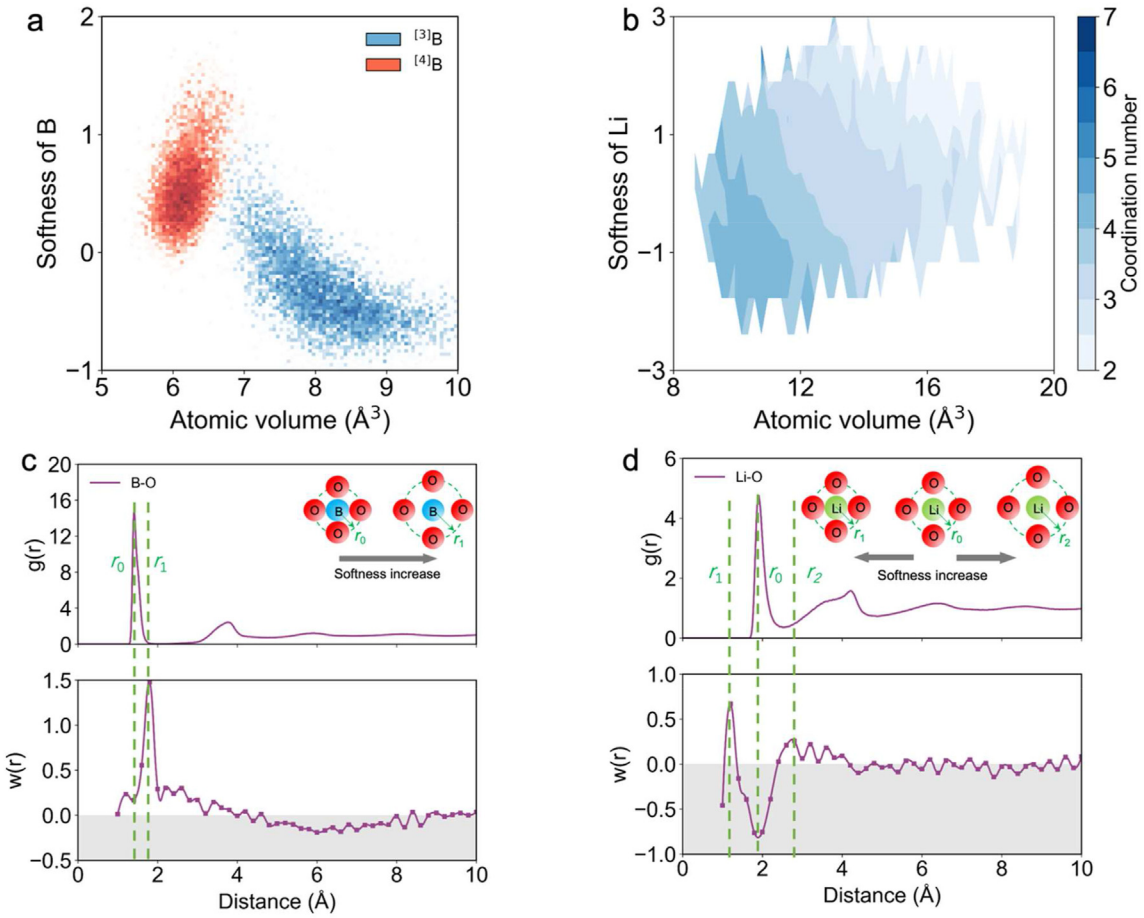

Fig. 5. (a,b) Softness of (a) B and (b) Li atoms as a function of their atomic volume and coordination number. (c,d) Weight coefficient w(r) of the classification hyperplane to calculate the softness of (c) B atoms and (d) Li atoms as a function of the radial distance. The partial pair distribution function of (c) B–O and (d) Li–O are provided at the top of each panel for reference.

most influential feature is associated with the distance $r_1 = 1.8$ Å. The average bond length of $^{[4]}$B–O is 1.52 Å, slightly higher than that of 1.41 Å of $^{[3]}$B atoms, in agreement with the literature [36]. As such, the B–O tetrahedra with the bond length of 1.8 Å (i.e., the largest B–O distance in the first coordination shell) are most likely to experience bond-switching activities. We also observe that $w(r)$ in the region of 5–8 Å exhibits a negative value, indicating that the MRO structure also influences the bond-switching activities. Specifically, the B atoms surrounded by other B atoms are less prone to change their CNs, while the B atoms are more likely to bond switch when surrounded by P atoms (Supporting Fig. S14).

For the softness of Li, $w(r)$ and the partial pair distribution function of different atomic pairs are shown in Fig. 5d and Supporting Fig. S15. We observe that the Li–Li correlation mostly facilitates the rearrangement of Li, as the $w(r)$ mainly shows a positive value, indicating that the accumulation of Li ions tends to exhibit good ion conduction. Since the accumulation of Li atoms typically exists within the larger ring structures, this echoes our previous finding that the relatively large rings facilitate Li ion migration [22]. The Li–P correlation exhibits the opposite trend to that of Li–Li, highlighting the steric hindrance effect of P on Li rearrangement. Similar to the case of B atoms, the most influential correlation is attributed to the Li–O pair, which has a strong Coulombic interaction. Fig. 5d shows that the effect of O on Li rearrangement is closely correlated with the interatomic distance. Specifically, when the Li–O distance equals the equilibrium position r_0, the Li atoms tend to be stabilized and thus exhibit low rearrangement. However, when the Li–O distance becomes shorter or longer than r_0, the softness of Li will increase since it is away from its equilibrium position. The comparison of $w(r)$ and the partial pair distribution functions highlights that the B or Li atoms with a high propensity to rearrangement are in out-of-equilibrium states, corresponding to a thermodynamically unstable states that tend to relax towards a lower energy state over time.

Finally, we investigate the softness evolution of B atoms during the fracture process. To this end, we calculate the softness of B as a function of applied strain at an interval of $\Delta\varepsilon = 0.01$. Although the classification hyperplane is built without the knowledge of the investigated samples, the calculated softness is able to capture the mechanical behaviors of the glassy LiBP electrolytes. As shown in Fig. 6a, the B atoms with different softness are uniformly distributed in the non-strained sample. Upon deformation to $\varepsilon = 0.2$, the softness of B generally decreases and especially in the vicinity of the crack. Fig. 6b shows the average softness of B atoms for different LiBP samples as a function of strain. Overall, the glasses with a higher P_2O_5 content tend to exhibit higher softness values of B atoms, indicating a higher propensity for bond-switching. Upon stretching, the softness will decrease initially and then increase after reaching the fracture strain, highlighting that softness is an indicator of fracture growth. We note that this evolution trend of softness is opposite to our previous findings of simulated glassy Al_2O_3 [25]. For glassy Al_2O_3, the softness is trained on the atomic rearrangement (i.e., the propensity to rearrange). However, in this work, softness is directly trained on the bond-switching property.

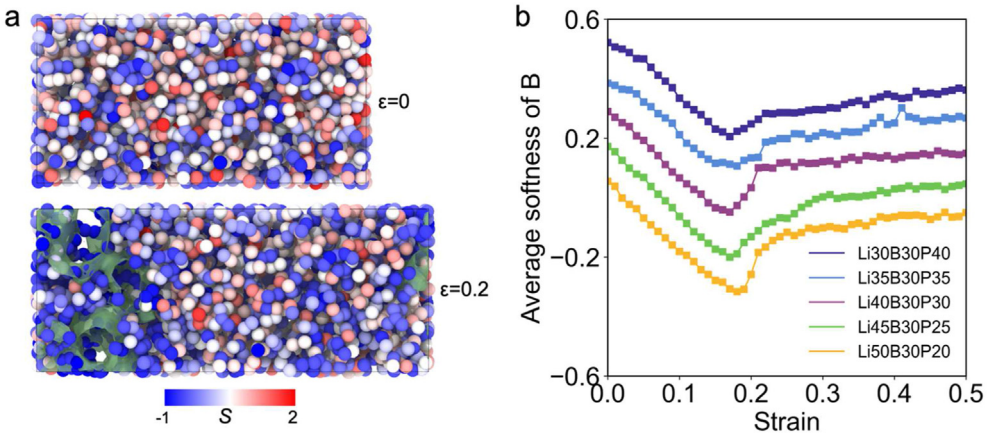

Fig. 6. Correlation of softness of B atoms and applied strain during fracture simulations. (a) Spatial distribution of particle softness of B atoms at different strain states. The B particles are colored based on the softness values. The fracture surfaces are colored green. (b) Average softness of B atoms as a function of the applied strain in the different LiBP glassy electrolytes.

From the evolution of softness, the initially decreased softness is attributed to the increased atomic volume and decreased CN of B atoms (see Fig. 5a) upon tension. After fracture, the increase in softness is attributed to the compression induced by the sudden release of stress, leading to the partial recovery of B coordination state and atomic volume. This is seen from the CN change as a function of the applied strain (Supporting Fig. S6).

3. Conclusions

In this work, we have applied the machine learning-based softness metric to understand the ionic conduction and fracture behavior of glassy lithium borophosphate electrolytes. The fracture propensity and ionic conduction are found to be correlated with the bond-switching behavior of B atoms and atomic rearrangement of Li atoms, respectively. These findings suggest that the long-term dynamics of both Li and B atoms at ambient conditions are largely encoded in the initial static glass structures. Namely, the long-term properties of glass structures can be forecasted without the time-consuming simulations. Based on the interpretability of the applied logistics regression classifier, the influences of structural features at different length scales on the long-term dynamics have been identified. Although the medium range structure plays a role in the softness calculation, the most influential factors are attributed to the first oxygen-coordination shell of Li ions. The out-of-equilibrium lengths of B—O or Li—O bonds empower the excess rearrangement of the atoms, i.e., they are the origin of the propensity for bond-switching or diffusion. The tuning of the B—O or Li—O bond lengths can, experimentally, be achieved by either post-treatment (such as hot compression) or compositional design (such as addition of alkali oxides to regulate the boron anomaly effect or packing density). The present results suggest that machine learning can be a powerful tool in revealing the hidden correlation between structural features and long-term dynamic behaviors. Consequently, the development of high-performance electrolyte materials with tailored properties can be achieved by tuning the atomic structure.

4. Methods

4.1. MD simulation of melt-quenched glass

We performed classical MD simulations of LiBP glassy electrolytes using the GPU-accelerated LAMMPS package [37]. The visualization of atomic configurations was performed using the OVITO package [38]. The interatomic interactions of atoms were described using a recently developed classical potential from Ref. [39] which is a combination of short-range Buckingham form and a long-range Coulombic term. This potential has been widely used in the simulations of different lithium-containing borate and phosphate systems, especially in reproducing the ionic conductivity and boron anomaly behaviors [40,41]. The detailed parameterization of this potential can be found in Ref. [39] and it has been thoroughly validated in our previous work on LiBP glasses [22]. The long-range Coulombic interactions were calculated using the particle-particle particle-mesh (PPPM) method with an accuracy of 10^{-5}. The motion of atoms was described by the velocity-Verlet algorithm with a timestep of 1 fs. For each composition, we prepared three samples by changing the initial temperature profile to ensure the reliability of the results. For example, the three different cases of Li40B30P30 glassy electrolytes exhibit a similar structure and fracture behavior (Supporting Fig. S17), indicating the reliability of the simulations.

We generated the atomic configurations of the LiBP glassy electrolytes through the conventional melt-quenching procedure following Chen et al. [22] Specifically, Li_2O, B_2O_3, and P_2O_5 units with designated numbers were randomly placed in an orthorhombic box using the PACKMOL package [42]. All the directions were simulated using periodic boundary conditions. Here, we simulated two series of LiBP glassy electrolytes with fixed B_2O_3 content and Li_2O content, respectively. The detailed composition and size of each system can be found in Supporting Table S1. For the Li40B40P30 sample, we simulated systems with five different sizes (around 3,000, 6,000, 10,000, 30,000, and 100,000 atoms) to investigate the system size effect. Both the glass structure and properties with the system size of 10,000 atoms can achieve a satisfactory accuracy when compared to the large system sizes (see Supporting Figs. S18 and S19). As such, the system size of around 10,000 atoms achieves a good balance between computational accuracy and efficiency, and we thus prepared all the samples were prepared with a similar system size of around 10,000 atoms.

The systems were melted at 3000 K in the canonical (*NVT*) ensemble for 50 ps to ensure the loss of any memory of the initial structure. These systems were cooled to 300 K in the isothermal—isobaric (*NPT*) ensemble under zero pressure at the cooling rate of 1 K/ps. The systems were subsequentially relaxed in the *NVT* and *NPT* ensemble at 300 K, respectively. The resulting configurations were further equilibrated in the *NVT* ensemble at

300 K for 100 ps to extract the trajectory for structural analysis. During the simulation, the temperature and pressure of the systems were controlled using the Nosé–Hoover [43] thermostat and barostat, respectively.

4.2. Structural analysis

The resulting structures of LiBP glassy electrolytes were analyzed by computing the pair distribution function (PDF) $g(r)$ and structural factor $S(Q)$. Specifically, we first computed the partial PDF g(r) [44].

$$g_{ij}(r) = \frac{\delta n_{ij}(r)}{4\pi r^2 dr \rho_j} \tag{1}$$

where $\delta n_{ij}(r)$ is the number of atoms of type j between distance r and r+dr from an atom of type i, and ρ_j is the average number density of atoms of type j. The differential correlation function D(r) was then calculated,

$$D(r) = 4\pi r \rho G(r) \tag{2}$$

$$G(r) = \sum_{i,j} c_i b_i c_j b_j \left(g_{ij}(r) - 1\right) \tag{3}$$

where b_i and b_j are the coherent bound neutron scattering length of species i and j (−1.90, 5.30, 5.803, 5.13 fm for Li, B, O, P, respectively [45]), c_i and c_j are the concentration of type i and j, respectively. Neutron weighted partial structure factor $S_{ij}(Q)$ of the simulated glasses were calculated using the Faber Ziman formalism [46].

$$S_{ij}(Q) = 1 + \rho_0 \int_0^{r_{max}} 4\pi r^2 \left(g_{ij}(r) - 1\right) \frac{\sin(Qr)}{Qr} \frac{\sin\left(\frac{\pi r}{r_{max}}\right)}{\frac{\pi r}{r_{max}}} dr \tag{4}$$

$$S(Q) = \frac{\sum_{i,j=1}^{n} c_i b_i c_j b_j S_{ij}(Q)}{\sum_{i,j=1}^{n} c_i b_i c_j b_j} \tag{5}$$

where Q is the scattering vector, r_{max} is the maximum distance of integration, here is around half the box size. The term $\sin\left(\frac{\pi r}{r_{max}}\right)/\frac{\pi r}{r_{max}}$ is a Lorch-type function used to reduce the ripples of $S_{ij}(Q)$ induced by the Fourier transformation with a finite cutoff r.

The atomic volumes of the atoms were calculated using the OVITO Voronoi analysis tool [38] from a Voronoi tessellation.

4.3. Fracture simulations

The obtained glass structures were subjected to uniaxial tensile deformation to analyze their deformation and fracture behaviors. The tensile simulations followed our previous work in Ref. [25] The simulated structures were duplicated in the x-direction to enable the loading to be applied to the longer direction. Before loading, the replicated structures were further equilibrated in the *NPT* ensemble at 300 K and zero pressure for 100 ps. To select an appropriate strain rate, we initially tested the stress-strain response with different strain rates for the Li40B40P30 sample (see Supporting Fig. S20). Although the simulation strain rate is much higher than that used in typical experiments, we find that the strain rate of 5×10^{10} s^{-1} can achieve a relatively accurate stress–strain response, as also reported in Ref. [47]. More importantly, the relative performance between the different samples is found to be independent of the applied strain rate (Supporting Fig. S21). Therefore, a constant strain rate of 5×10^{10} s^{-1} was selected for the fracture simulations along the x-direction. During the tensile process, the system was maintained at 300 K, while the lateral directions were kept at zero stress (i.e., plane stress conditions). The trajectory during the tensile process was recorded at a strain interval of 0.001, while the stress component in the x-direction and corresponding strain were extracted for stress-strain analysis.

4.4. Bond-switching analysis

The fracture behavior of the samples was correlated with the atomic arrangement associated with bond breaking and reformation processes. That is, the changes in coordination number and bond-switching activities were analyzed during the tensile deformation. The coordination numbers were first analyzed by calculating the partial pair distribution functions. The cutoffs of B–O and P–O pairs were determined as the distance at the minimum after the first peak in the corresponding pair distribution functions (Supporting Fig. S2). The atom pairs were considered to be bonded if they were within the cutoff distance. Specifically, the cutoffs of B–O and P–O pairs were both selected to be 2.0 Å, and the CN of B and P was determined as the number of O atoms within the cutoff.

The bond-switching analysis was then performed to calculate the fraction of atoms with an increased, decreased, swapped, or unchanged CN compared to the initial non-strained structure. This was achieved by comparing the CN of each individual atom and the identity of the neighboring atom with their initial non-strained state. If the CN has decreased or increased, then the atoms were labeled as Decreased CN or Increased CN, respectively. If the neighboring atoms remain unchanged, then the atoms were labeled as Unchanged CN. Otherwise, the atoms were marked as Swapped CN, denoting that the CNs of the atoms remained unchanged but at least one neighboring atom had been swapped.

4.5. Displacement analysis of Li atoms

The ion conduction of the glassy electrolytes was estimated by calculating the mean squared displacement (MSD). The as-prepared configurations were equilibrated in the *NVT* ensemble at either 300 K or 800 K for 1 ns to generate trajectories for MSD calculations. Then, MSD was calculated as,

$$\mathrm{MSD}_i(t) = \Delta r_i^2(t) = |r_i(t) - r_i(0)|^2 \tag{6}$$

where $r_i(t)$ is the position vector of the ith atom at time t. The average MSD of Li atoms was used to characterize the ion conduction in the LiBP electrolytes since the slope of MSD is correlated with the self-diffusion coefficient, which can be measured experimentally [30].

The atom-based arrangement of each Li was investigated by calculating the cumulative non-affine displacement D_{cum} at 300 K. The idea of non-affine squared displacement D^2_{min} is to isolate the atomic displacements from the reorganization of the neighboring deformation, and it has been widely used to describe atomic rearrangement processes [29,48]. The D_{cum} value of each Li atom is the sum of the square-root of the incremental non-affine displacements $\Delta D^2_{i,min}$ during the isothermal relaxation with each small increment of time. Following the literature [24,49], the D^2_{min} between times t and $t + \Delta t$ can be calculated as,

$$D^2_{\min} = \frac{1}{M_k}\sum_i^{M_k}[\boldsymbol{r}_{ik}(t+\Delta t) - \boldsymbol{J}_k(t)\boldsymbol{r}_{ik}(t)]^2 \quad (7)$$

where $\boldsymbol{r}_{ik}(t)$ is the displacement vector between atom i and j at time t, $\boldsymbol{J}_k(t)$ is the local strain tensor about atom k that minimizes $D^2_{\min}(k;t)$, M_k is the total number of neighboring atoms around atom k.

$$D_{cum} = \sum_{i=1}^{n}\sqrt{\Delta D^2_{i,\min}} \quad (8)$$

where $\Delta D^2_{i,\min}$ is the increment of D^2_{min} with Δt, while n is the total number of intervals during the 1 ns equilibration. The cut-off used for the calculation of $D^2_{\min}$ was set to 4 Å, which covers the first and second coordination shells of Li atoms. Although the difference in cut-off influences the values of D_{cum}, the relative behaviors between different compositions are not influenced by the cut-off values as seen in Supporting Fig. S22.

4.6. Machine learning classification

We adopt the machine learning-based "softness" metric to analyze the non-strained structure following the procedure proposed in Ref. [26] Unlike the initially proposed softness concept [24,29], here the softness calculation relies on the utilization of a logistic regression classifier rather than the support vector machine, since we found it to offer superior classification accuracy and training efficiency. Similar to previous studies, softness is defined as the distance to the hyperplane in the feature space as shown in Fig. 4a. Note that the previous findings [25,26,50] evidence that the radial order function dominates the prediction for atomic dynamics of systems simulated using two-body interactions (e.g., Buckingham potential). Therefore, the radial order parameters are selected as the features for constructing the hyperplane. The hyperplane created by logistic regression can be expressed as a function of each of the features as,

$$\sum_r w(r)G(i;r) - b = 0 \quad (9)$$

where the features $G(i;r)$ are standardized radial order parameters as a function of pairwise distance r, while $w(r)$ and b are the weight coefficients and bias of the logistic regression model, respectively. Therefore, the hyperplane is a linear combination of input features, which enables the softness to be informed with different features. Namely, the absolute value of $w(r)$ denotes the importance of the corresponding feature $G(i;r)$. The positive and negative signs of $w(r)$ thus indicate that the increasing values of $G(i;r)$ tend to increase and decrease the softness values, respectively.

For comparison, we also applied different regressor models to correlate the structural features with Li rearrangements. To this end, we used the datasets from LiBP glassy electrolytes with fixed Li_2O content ($(Li_2O)_{40}(B_2O_3)_{30+x}(P_2O_5)_{30-x}$) where $x = -10$, -5, 5, and 10 serves as training sets and $x = 0$ servess as the test set. As shown in Supporting Fig. S23, we used six different regressors, namely, support vector regression (SVR), bagging regressor (BR), gradient boosting regressor (GBR), random forest regressor (RFR), KNeighbors regressor (KNN), and multi-layer perceptron regressor (MLP). We find that the regression models do not exhibit satisfactory predictions in the test sets, indicating that the general regression algorithms cannot well capture the structure correlation with atomic rearrangement. This further motivates the present approach using a classification-based machine learning model.

To analyze the ionic conduction and fracture behavior, we trained two logistic regression (LR) models to calculate the softness in two different ways. That is, the outputs of the LR models were selected to be the D_{cum} metric of each Li atom and bond-switching rate of each B atom, respectively. To exclude the effect of atom numbers in influencing bulk properties, we keep the number of Li and B atoms fixed for analyzing the ionic conductivity and fracture behavior, respectively. To this end, the initial configurations of LiBP electrolytes were divided into two groups, i.e., the LR model of Li was trained on the $(Li_2O)_{40\text{-}x}(B_2O_3)_{30}(P_2O_5)_{30+x}$ samples, while the LR model of B was trained on the $(Li_2O)_{40}$ $(B_2O_3)_{30\text{-}x}(P_2O_5)_{30+x}$ ($x = -10$, -5, 5, and 10) samples. The one overlapping composition of $(Li_2O)_{40}(B_2O_3)_{30}(P_2O_5)_{30}$ serves as the test set for both the classification models for Li and B prediction to ensure the absence of data leakage.

To choose the features $G(i;r)$ for training, we first optimized the interval dr and cutoff Rc values of the radial order parameters. To this end, we examined the classification accuracy of the logistic hyperplane as a function of different combinations of dr and Rc values to discriminate the mobile and immobile B atoms as shown in Supporting Fig. S24. Based on this analysis, the values dr of 0.2 and Rc of 10 were selected to construct the structural features, which yielded a predicting accuracy of the test set of around 0.77 (a satisfactory accuracy when compared to our previous results solely used radial function [26,50]). Additionally, the dependence of classification accuracy of Li atoms on the cumulative non-affine displacement threshold Dc is shown in Supporting Fig. S25, which highlighted that a Dc value of 360 Å generated a similar accuracy of around 0.73 for both the training and test sets. Around 30% Li atoms was treated as mobile when we used a Dc value of 360 Å (Supporting Fig. S26). The confusion matrix for the prediction models for both B and Li can be found in Supporting Fig. S27. After the construction of the classification hyperplane, the softness of Li and B was calculated to predict whether an atom is prone to diffuse or undergo bond-switching, respectively.

CRediT authorship contribution statement

Tao Du: Conceptualization, Investigation, Formal analysis, Writing – Original Draft. **Zhimin Chen:** Investigation, Formal analysis, Writing – Review & Editing. **Han Liu:** Investigation, Writing – Review & Editing. **Qi Zhang:** Investigation, Writing – Review & Editing. **Mathieu Bauchy:** Conceptualization, Writing – Review & Editing. **Yuanzheng Yue:** Conceptualization, Writing – Review & Editing. **Morten M. Smedskjaer:** Conceptualization, Supervision, Writing – Original Draft.

Declaration of competing interest

The authors declare that they have no known competing financial interests or personal relationships that could have appeared to influence the work reported in this paper.

Data availability

Data will be made available on request.

Acknowledgments

This work was supported by Marie Skłodowska-Curie Individual Fellowship (101018156) to T.D, China Scholarship Council (202106880010) to Z.C., Independent Research Fund Denmark (1127–00003) to M.M.S, and National Science Foundation (DMR-1928538, DMR-1944510) to M.B. We also thank Danish e-infrastructure Cooperation (DeiC) National HPC (DeiC-AAU-N5-202200005) and Aalborg University (CLAAUDIA) for providing the computational resources.

Appendix A. Supplementary data

Supplementary data to this article can be found online at https://doi.org/10.1016/j.mtener.2023.101390.

References

[1] J.-M. Tarascon, M. Armand, Issues and challenges facing rechargeable lithium batteries, Nature 414 (2001) 359–367, https://doi.org/10.1038/35104644.
[2] S. Chu, A. Majumdar, Opportunities and challenges for a sustainable energy future, Nature 488 (2012) 294–303, https://doi.org/10.1038/nature11475.
[3] B. Scrosati, J. Hassoun, Y.-K. Sun, Lithium-ion batteries. A look into the future, Energy Environ. Sci. 4 (2011) 3287, https://doi.org/10.1039/c1ee01388b.
[4] P. Albertus, S. Babinec, S. Litzelman, A. Newman, Status and challenges in enabling the lithium metal electrode for high-energy and low-cost rechargeable batteries, Nat. Energy 3 (2018) 16–21, https://doi.org/10.1038/s41560-017-0047-2.
[5] P.G. Bruce, S.A. Freunberger, L.J. Hardwick, J.-M. Tarascon, Li–O2 and Li–S batteries with high energy storage, Nat. Mater. 11 (2012) 19–29, https://doi.org/10.1038/nmat3191.
[6] M. Armand, J.-M. Tarascon, Building better batteries, Nature 451 (2008) 652–657, https://doi.org/10.1038/451652a.
[7] M. Balaish, J.C. Gonzalez-Rosillo, K.J. Kim, Y. Zhu, Z.D. Hood, J.L.M. Rupp, Processing thin but robust electrolytes for solid-state batteries, Nat. Energy 6 (2021) 227–239, https://doi.org/10.1038/s41560-020-00759-5.
[8] D. Ravaine, Glasses as solid electrolytes, J. Non-Cryst. Solids 38–39 (1980) 353–358, https://doi.org/10.1016/0022-3093(80)90444-5.
[9] X. Yang, X. Li, K. Adair, H. Zhang, X. Sun, Structural design of lithium–sulfur batteries: from fundamental research to practical application, Electrochem. Energy Rev. 1 (2018) 239–293, https://doi.org/10.1007/s41918-018-0010-3.
[10] N.S. Saetova, A.A. Raskovalov, B.D. Antonov, T.V. Yaroslavtseva, O.G. Reznitskikh, N.I. Kadyrova, The influence of lithium oxide concentration on the transport properties of glasses in the Li2O–B2O3–SiO2 system, J. Non-Cryst. Solids 443 (2016) 75–81, https://doi.org/10.1016/j.jnoncrysol.2016.04.025.
[11] S.-K. Jung, H. Gwon, G. Yoon, L.J. Miara, V. Lacivita, J.-S. Kim, Pliable lithium superionic conductor for all-solid-state batteries, ACS Energy Lett. 6 (2021) 2006–2015, https://doi.org/10.1021/acsenergylett.1c00545.
[12] J.S. Kim, S. Jung, H. Kwak, Y. Han, S. Kim, J. Lim, Y.M. Lee, Y.S. Jung, Synergistic halide-sulfide hybrid solid electrolytes for Ni-rich cathodes design guided by digital twin for all-solid-State Li batteries, Energy Storage Mater. 55 (2023) 193–204, https://doi.org/10.1016/j.ensm.2022.11.038.
[13] K.I. Cho, S.H. Lee, K.H. Cho, D.W. Shin, Y.K. Sun, Li2O–B2O3–P2O5 solid electrolyte for thin film batteries, J. Power Sources 163 (2006) 223–228, https://doi.org/10.1016/j.jpowsour.2006.02.011.
[14] A. Magistris, G. Chiodelli, M. Villa, Lithium borophosphate vitreous electrolytes, J. Power Sources 14 (1985) 87–91, https://doi.org/10.1016/0378-7753(85)88016-2.
[15] R. Koerver, W. Zhang, L. de Biasi, S. Schweidler, A.O. Kondrakov, S. Kolling, T. Brezesinski, P. Hartmann, W.G. Zeier, J. Janek, Chemo-mechanical expansion of lithium electrode materials – on the route to mechanically optimized all-solid-state batteries, Energy Environ. Sci. 11 (2018) 2142–2158, https://doi.org/10.1039/C8EE00907D.
[16] A. Manthiram, X. Yu, S. Wang, Lithium battery chemistries enabled by solid-state electrolytes, Nat. Rev. Mater. 2 (2017) 16103, https://doi.org/10.1038/natrevmats.2016.103.
[17] K.I. Cho, S.H. Lee, D.W. Shin, Y.K. Sun, Relationship between glass network structure and conductivity of Li2O–B2O3–P2O5 solid electrolyte, Electrochim. Acta 52 (2006) 1576–1581, https://doi.org/10.1016/j.electacta.2006.02.065.
[18] Y. Yoon, C. Park, J. Kim, D. Shin, Characterization of lithium borophosphate glass thin film electrolytes deposited by RF-magnetron sputtering for micro-batteries, Solid State Ionics 225 (2012) 636–640, https://doi.org/10.1016/j.ssi.2012.05.008.
[19] B.K. Money, K. Hariharan, Glass formation and electrical conductivity studies of melt quenched and mechanically milled 50Li2O:(50−x) P2O5:xB2O3, Solid State Ionics 179 (2008) 1273–1277, https://doi.org/10.1016/j.ssi.2007.12.068.
[20] F. Muñoz, L. Montagne, L. Pascual, A. Durán, Composition and structure dependence of the properties of lithium borophosphate glasses showing boron anomaly, J. Non-Cryst. Solids 355 (2009) 2571–2577, https://doi.org/10.1016/j.jnoncrysol.2009.09.013.
[21] C.E. Athanasiou, X. Liu, M.Y. Jin, E. Nimon, S. Visco, C. Lee, M. Park, J. Yun, N.P. Padture, H. Gao, B.W. Sheldon, Rate-dependent deformation of amorphous sulfide glass electrolytes for solid-state batteries, Cell Rep. Phys. Sci. 3 (2022) 100845, https://doi.org/10.1016/j.xcrp.2022.100845.
[22] Z. Chen, T. Du, S.S. Sørensen, R. Christensen, Q. Zhang, L.R. Jensen, O.V. Magdysyuk, M. Diaz-Lopez, M. Bauchy, Y. Yue, M.M. Smedskjaer, Structure dependence of fracture toughness and ionic conductivity in lithium borophosphate glassy electrolytes for all-solid-state batteries, J. Power Sources 553 (2023) 232302, https://doi.org/10.1016/j.jpowsour.2022.232302.
[23] S.S. Schoenholz, E.D. Cubuk, D.M. Sussman, E. Kaxiras, A.J. Liu, A structural approach to relaxation in glassy liquids, Nat. Phys. 12 (2016) 469–471, https://doi.org/10.1038/nphys3644.
[24] E.D. Cubuk, R.J.S. Ivancic, S.S. Schoenholz, D.J. Strickland, A. Basu, Z.S. Davidson, J. Fontaine, J.L. Hor, Y.-R. Huang, Y. Jiang, N.C. Keim, K.D. Koshigan, J.A. Lefever, T. Liu, X.-G. Ma, D.J. Magagnosc, E. Morrow, C.P. Ortiz, J.M. Rieser, A. Shavit, T. Still, Y. Xu, Y. Zhang, K.N. Nordstrom, P.E. Arratia, R.W. Carpick, D.J. Durian, Z. Fakhraai, D.J. Jerolmack, D. Lee, J. Li, R. Riggleman, K.T. Turner, A.G. Yodh, D.S. Gianola, A.J. Liu, Structure-property relationships from universal signatures of plasticity in disordered solids, Science 358 (2017) 1033–1037, https://doi.org/10.1126/science.aai8830.
[25] T. Du, H. Liu, L. Tang, S.S. Sørensen, M. Bauchy, M.M. Smedskjaer, Predicting fracture propensity in amorphous alumina from its static structure using machine learning, ACS Nano 15 (2021) 17705–17716, https://doi.org/10.1021/acsnano.1c05619.
[26] H. Liu, S. Xiao, L. Tang, E. Bao, E. Li, C. Yang, Z. Zhao, G. Sant, M.M. Smedskjaer, L. Guo, M. Bauchy, Predicting the early-stage creep dynamics of gels from their static structure by machine learning, Acta Mater. 210 (2021) 116817, https://doi.org/10.1016/j.actamat.2021.116817.
[27] Q. Wang, L. Zhang, Inverse design of glass structure with deep graph neural networks, Nat. Commun. 12 (2021) 5359, https://doi.org/10.1038/s41467-021-25490-x.
[28] Z. Fan, E. Ma, Predicting orientation-dependent plastic susceptibility from static structure in amorphous solids via deep learning, Nat. Commun. 12 (2021) 1506, https://doi.org/10.1038/s41467-021-21806-z.
[29] E.D. Cubuk, S.S. Schoenholz, J.M. Rieser, B.D. Malone, J. Rottler, D.J. Durian, E. Kaxiras, A.J. Liu, Identifying structural flow defects in disordered solids using machine-learning methods, Phys. Rev. Lett. 114 (2015) 108001, https://doi.org/10.1103/PhysRevLett.114.108001.
[30] K.-L. Tung, K.-S. Chang, C.-C. Hsiung, Y.-C. Chiang, Y.-L. Li, Molecular dynamics simulation of the complex dopant effect on the super-ionic conduction and microstructure of zirconia-based solid electrolytes, Sep. Purif. Technol. 73 (2010) 13–19, https://doi.org/10.1016/j.seppur.2009.07.026.
[31] P. Liu, R.E. Youngman, L.R. Jensen, M.M. Smedskjaer, Correlating structure with mechanical properties in lithium borophosphate glasses, Int. J. Appl. Glass Sci. 14 (2023) 38–51, https://doi.org/10.1111/ijag.16592.
[32] E.J. Frankberg, J. Kalikka, F.G. Ferré, L. Joly-Pottuz, T. Salminen, J. Hintikka, M. Hokka, S. Koneti, T. Douillard, B.L. Saint, P. Kreiml, M.J. Cordill, T. Epicier, D. Stauffer, M. Vanazzi, L. Roiban, J. Akola, F.D. Fonzo, E. Levänen, K. Masenelli-Varlot, Highly ductile amorphous oxide at room temperature and high strain rate, Science 366 (2019) 864–869, https://doi.org/10.1126/science.aav1254.
[33] T. Du, H. Li, Q. Zhou, Z. Wang, G. Sant, J.V. Ryan, M. Bauchy, Atomistic origin of the passivation effect in hydrated silicate glasses, npj Mater. Degrad. 3 (2019) 6, https://doi.org/10.1038/s41529-019-0070-9.
[34] C. Hermansen, R.E. Youngman, J. Wang, Y. Yue, Structural and topological aspects of borophosphate glasses and their relation to physical properties, J. Chem. Phys. 142 (2015) 184503, https://doi.org/10.1063/1.4919798.
[35] X. Ma, Z.S. Davidson, T. Still, R.J.S. Ivancic, S.S. Schoenholz, A.J. Liu, A.G. Yodh, Heterogeneous activation, local structure, and softness in supercooled colloidal liquids, Phys. Rev. Lett. 122 (2019) 028001, https://doi.org/10.1103/PhysRevLett.122.028001.
[36] L. Pedesseau, S. Ispas, W. Kob, First-principles study of a sodium borosilicate glass-former. II. The glass state, Phys. Rev. B 91 (2015) 134202, https://doi.org/10.1103/PhysRevB.91.134202.
[37] S. Plimpton, Fast parallel algorithms for short-range molecular dynamics, J. Comput. Phys. 117 (1995) 1–19, https://doi.org/10.1006/jcph.1995.1039.
[38] A. Stukowski, Visualization and analysis of atomistic simulation data with OVITO–the Open Visualization Tool, Model. Simulat. Mater. Sci. Eng. 18 (2009) 015012, https://doi.org/10.1088/0965-0393/18/1/015012.
[39] L. Deng, J. Du, Development of boron oxide potentials for computer simulations of multicomponent oxide glasses, J. Am. Ceram. Soc. 102 (2019) 2482–2505, https://doi.org/10.1111/jace.16082.
[40] S.S. Sørensen, H. Johra, J.C. Mauro, M. Bauchy, M.M. Smedskjaer, Boron anomaly in the thermal conductivity of lithium borate glasses, Phys. Rev. Mater. 3 (2019) 075601, https://doi.org/10.1103/PhysRevMaterials.3.075601.
[41] P.H. Kuo, J. Du, Lithium ion diffusion mechanism and associated defect behaviors in crystalline Li $_{1+x}$ Al $_x$ Ge $_{2-x}$ (PO $_4$) $_3$ solid-state electrolytes, J. Phys. Chem. C 123 (2019) 27385–27398, https://doi.org/10.1021/acs.jpcc.9b08390.
[42] L. Martínez, R. Andrade, E.G. Birgin, J.M. Martínez, PACKMOL: a package for building initial configurations for molecular dynamics simulations, J. Comput. Chem. 30 (2009) 2157–2164, https://doi.org/10.1002/jcc.21224.
[43]] S. Nosé, A molecular dynamics method for simulations in the canonical ensemble, Mol. Phys. 52 (1984) 255–268, https://doi.org/10.1080/00268978400101201.
[44] D.A. Keen, A comparison of various commonly used correlation functions for describing total scattering, J. Appl. Crystallogr. 34 (2001) 172–177, https://doi.org/10.1107/S0021889800019993.
[45] V.F. Sears, Neutron scattering lengths and cross sections, Neutron News 3 (1992) 26–37, https://doi.org/10.1080/10448639208218770.
[46] T.E. Faber, J.M. Ziman, A theory of the electrical properties of liquid metals, Philos. Mag. J. Theor. Exp. Appl. Phys. 11 (1965) 153–173, https://doi.org/10.1080/14786436508211931.

[47] S.C. Chowdhury, B.Z. (Gama) Haque, J.W. Gillespie, Molecular dynamics simulations of the structure and mechanical properties of silica glass using ReaxFF, J. Mater. Sci. 51 (2016) 10139–10159, https://doi.org/10.1007/s10853-016-0242-8.

[48] A. Sierou, J.F. Brady, Shear-induced self-diffusion in non-colloidal suspensions, J. Fluid Mech. 506 (2004) 285–314, https://doi.org/10.1017/S0022112004008651.

[49] M.L. Falk, J.S. Langer, Dynamics of viscoplastic deformation in amorphous solids, Phys. Rev. E. 57 (1998) 7192–7205, https://doi.org/10.1103/PhysRevE.57.7192.

[50] H. Liu, M.M. Smedskjaer, M. Bauchy, Deciphering a structural signature of glass dynamics by machine learning, Phys. Rev. B 106 (2022) 214206, https://doi.org/10.1103/PhysRevB.106.214206.